THE UNIVERSITY of EDINBURGH

Edinburgh Research Explorer

Cs3Bi2I9 as high-performance electrode material achieving high capacitance and stability in an economical supercapacitor

Citation for published version:
Adams, K, Mallows, J, Li, T, Kampouris, D, Thijssen, JHJ & Robertson, N 2019, 'Cs3Bi2I9 as high-performance electrode material achieving high capacitance and stability in an economical supercapacitor', *JPhys Energy*. https://doi.org/10.1088/2515-7655/ab22d7

Digital Object Identifier (DOI):
10.1088/2515-7655/ab22d7

Link:
Link to publication record in Edinburgh Research Explorer

Document Version:
Peer reviewed version

Published In:
JPhys Energy

General rights
Copyright for the publications made accessible via the Edinburgh Research Explorer is retained by the author(s) and / or other copyright owners and it is a condition of accessing these publications that users recognise and abide by the legal requirements associated with these rights.

Take down policy
The University of Edinburgh has made every reasonable effort to ensure that Edinburgh Research Explorer content complies with UK legislation. If you believe that the public display of this file breaches copyright please contact openaccess@ed.ac.uk providing details, and we will remove access to the work immediately and investigate your claim.

Download date: 08. May. 2023

$Cs_3Bi_2I_9$ as high-performance electrode material achieving high capacitance and stability in an economical supercapacitor

Keir Adams[1], John Mallows[1], Tianyue Li[1*], Dimitrios Kampouris[1], Job H. J. Thijssen[2] and Neil Robertson[1*]

[1] EaStCHEM School of Chemistry, The University of Edinburgh, Edinburgh, EH9 3FJ, UK
[2] SUPA School of Physics & Astronomy, The University of Edinburgh, Edinburgh, EH9 3FD, UK

E-mail: Neil.Robertson@ed.ac.uk, Tianyue.Li@ed.ac.uk

Received xxxxxx
Accepted for publication xxxxxx
Published xxxxxx

Abstract

Supercapacitors are well-known as promising energy storage devices capable of bridging the gap between conventional electrolytic capacitors and batteries to deliver both high power and energy densities for applications in electric vehicles and a smart energy grid. However, many reported instances of high-capacitance pseudocapacitors employ strong Faradaic reactions that hinder fast charge-discharge cycles and long-term stability, limiting their commercial viability. In this study, we utilize an economical and solution-processable procedure to fabricate a $Cs_3Bi_2I_9$-based symmetric supercapacitor employing both electric double layer capacitance and pseudocapacitance with an aqueous $NaClO_4$ electrolyte to deliver an outstanding device areal capacitance of 2.4 F cm^{-2} and specific capacitance of 280 F g^{-1}. The $Cs_3Bi_2I_9$ device achieves an excellent 88% capacitance retention after 5000 charge-discharge cycles, proving its long-term cycle stability and promise as a practical supercapacitor. We characterize the time-dependent charge storage mechanisms through cyclic voltammetry and electrochemical impedance spectroscopy to find that electrostatic charge accumulation predominates at high potentials (0.3-0.6 V) whereas weak, Faradaic charge adsorption and pore penetration bolster charge storage at lower potentials (0.0-0.2 V).

Keywords: supercapacitor, bismuth, impedance

1. Introduction

The recent proliferation of renewable but variable solar and wind energy technologies, as well as the growing market for hybrid electric vehicles, has spurred research efforts to develop a new generation of high performing and sustainable energy storage devices.[1-3] So-called supercapacitors (ultracapacitors, electrochemical capacitors) have accrued particular research attention for their high energy densities compared to conventional capacitors and rapid charge-discharge rates and long-life cycle stabilities compared to batteries and fuel cells.[4-7] Supercapacitors can be subdivided into two classifications depending on their predominant charge storage mechanism: electric double layer capacitors (EDLC) store charge primarily through non-Faradaic electrostatic interactions between a polarized electrolyte and charged electrodes, whereas pseudocapacitors combine the electrostatic behaviour of EDLCs with typically reversible Faradaic reactions between the electrolytic solution and the electrode surface, which is often coated with metal oxides and other inorganic/organic hybrid materials.[8-10] While EDLCs

 © xxxx IOP Publishing Ltd

boast optimal power densities and long-life stabilities necessary for commercial applications due to the highly-reversible nature of electrostatic charge storage, EDLCs often lack suitable energy densities for real world applications.[11,12] In contrast, pseudocapacitors can achieve capacitances 10-100 times greater than EDLCs while preserving high power densities by constraining electron transfer to the electrodes' surfaces and near-surface pores.[13,14] Popular pseudocapacitor electrode materials have included RuO_2, MnO_2, and other inorganic/organic hybrids that acclaim extremely high gravimetric capacitances (> 1000 F g^{-1}) and areal capacitances (>100 mF cm^{-2}).[15-22] Many such pseudocapacitive materials however, undergo strong Faradaic reactions that inhibit long-term stability and prevent fast discharge.[23] Furthermore, claims of deceptively ultrahigh gravimetric capacitances are often calculated from electrodes with extremely low mass loadings (<1 mg cm^{-2}) that cannot be scaled to attain durable and high-capacitance electrodes for their advertised commercial applications.[24, 25, 12]

Consequently, there exists a strong incentive to fabricate and characterize a new class of electrode materials that maintain high energy and power densities by employing some Faradaic reactions in conjunction with strong electric double layer capacitance and larger mass-loadings that can be more realistically implemented in commercial devices. Recently, main-group halide compounds, related to perovskites utilized in photovoltaics, with formula $A_3M_2X_9$ where A is an organic/inorganic cation, M is a high-Z ns^2 metal cation, and X is a halogen have proven to be promising candidates for active supercapacitor electrode materials.[26-30] Zhou and colleagues fabricated a $(CH_3NH_3)Pb_2I_9$-based EDLC using $(CH_3NH_3)Pb_2I_9$ – coated FTO electrodes that achieved a device areal capacitance of 5.89 μF cm^{-2},[29] while Pious and colleagues, noting the toxicity of lead, reported a single-electrode areal capacitance of 5.5 mF cm^{-2} (equivalent to a device areal capacitance of 2.25 mF cm^{-2}) for an EDLC using $(CH_3NH_3)Bi_2I_9$–coated carbon cloth as the electrodes.[30] This impressive 1000 fold increase in areal capacitance indicates the promising nature of perovskite–like, bismuth–based complexes for electrochemical energy storage devices. We previously fabricated a symmetric EDLC-type supercapacitor using electrodes coated with solution-deposited $Bi_{13}S_{18}I_2$ and aqueous $NaClO_4$ electrolyte that achieved a systemic areal capacitance of 211 mF cm^{-2}.[31] This additional order-of-magnitude improvement we achieved in the capacitance of bismuth iodide–based complexes encourages further optimization of solution-processable bismuth–based supercapacitors as well as investigation into their charge storage mechanisms.

In this paper, we present a facile and economical fabrication of a $Cs_3Bi_2I_9$-based symmetrical supercapacitor that employs EDLC-type charge storage at high potentials

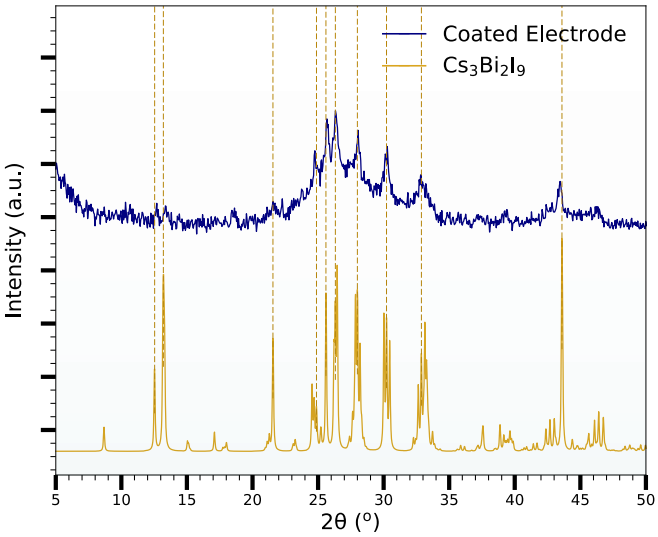

Figure 1. XRD pattern for the $Cs_3Bi_2I_9$ – coated electrode (blue) compared with the theoretical XRD pattern for pure powder $Cs_3Bi_2I_9$ (gold) calculated from CCDC Mercury software (ICSD data base for coll. code 1448).[32]

along with Faradaic charge adsorption/desorption and pore penetration at low potentials. We electrochemically characterize the device's capacitive performance through cyclic voltammetry, galvanostatic charge-discharge measurements, and AC electrochemical impedance spectroscopy. The fabricated electrodes exhibit an acceptable mass loading (3.9 mg cm^{-2} each) of activated $Cs_3Bi_2I_9$ material preferable for large-scale commercialization, and the electrodes are characterized by SEM, XRD, and Raman spectroscopy. The device, consisting of two electrodes in series, achieves commendable maximum areal and specific capacitances of 2.4 F cm^{-2} and 280 F g^{-1}, which represent orders of magnitude greater capacitance compared to the reported $(CH_3NH_3)Bi_2I_9$-based EDLC.[30] The supercapacitor also retains an excellent 88% of its initial capacitance even after 5000 charge-discharge cycles at a large current density of 2 A g^{-1}, proving the long-term stability of the fabricated $Cs_3Bi_2I_9$-based electrodes. Overall, the economical fabrication, superior capacitance, and outstanding cycle stability of the $Cs_3Bi_2I_9$ prove its excellent performance as the active supercapacitor electrode material.

2. Results and Discussion

2.1 Electrode fabrication and characterization

The $Cs_3Bi_2I_9$-based electrodes were fabricated from solution in a single step. A 3:2 molar ratio of CsI and BiI_3 was first mixed together with activated charcoal and polytetrafluroethylene (PTFE) powder in an 85:10:5 weight ratio ($Cs_3Bi_3I_9$:charcoal:PTFE) , to which DMF was added to form a suspended, heterogeneous solution. This solution was

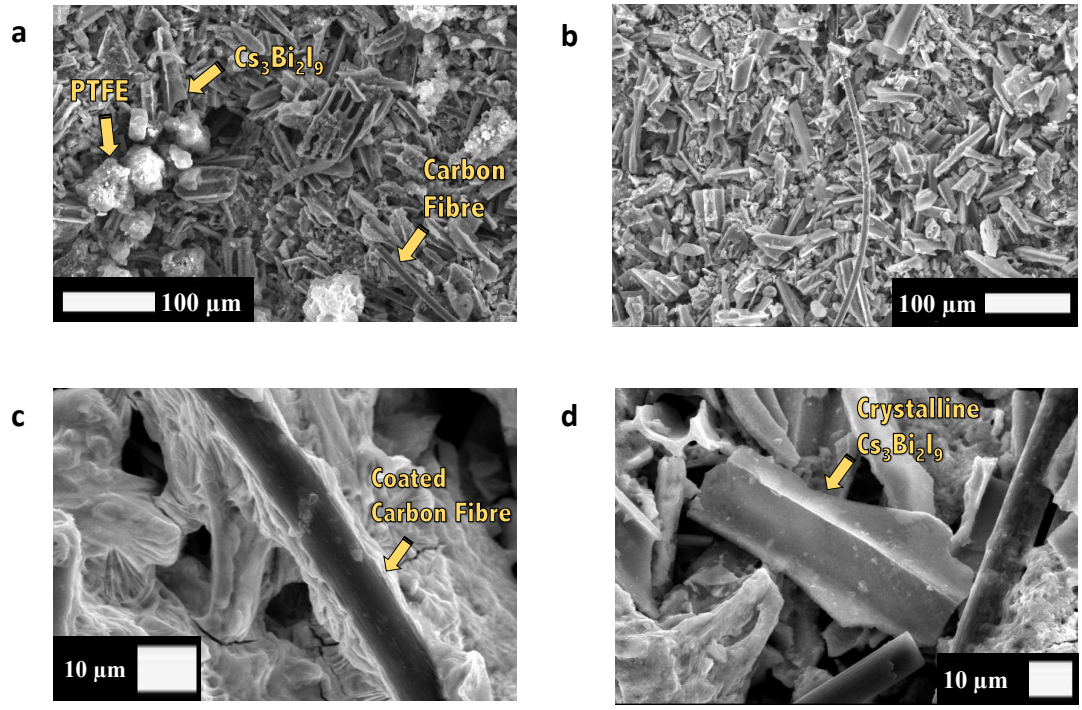

Figure 2. SEM images for the coated electrodes showing (a) heterogeneity of surface and amorphous PTFE, (b) good surface coverage of the carbon cloth, (c) crystalline $Cs_3Bi_2I_9$ layering on top of the carbon cloth, and (d) $Cs_3Bi_2I_9$ with well-formed crystalline shape coating the carbon cloth fibres.

thoroughly dispersed and drop-cast on 1 cm^2 squares of carbon cloth, which were subsequently annealed at 150 ^oC for 1 hour on a hot plate to crystallize $Cs_3Bi_2I_9$ directly on the carbon cloth substrate with a high mass loading of 3.9 mg cm^{-2}. The electrodes were characterized through X-ray diffraction (XRD) and scanning electron microscopy (SEM). Figure 1 compares the XRD pattern of the as-made $Cs_3Bi_2I_9$-based electrodes with the calaculated pattern for powder $Cs_3Bi_2I_9$. The electrodes exhibit clear peaks around 13^o, 22^o, 25-28^o, 30^o, 33^o, 39^o, 44^o, and 46^o on a 2θ scale that correspond very closely with the positions of the calculated $Cs_3Bi_2I_9$ peaks. Although the mesoscopic structure and inhomogeneity of the prepared $Cs_3Bi_2I_9$ – coated electrodes produce broadened XRD peaks with lower signal to noise ratio compared to the theoretical $Cs_3Bi_2I_9$ powder, the positional agreement between the experimental and theoretical patterns suggests high crystallinity and purity of the $Cs_3Bi_2I_9$ active layer and excellent coverage of the carbon cloth substrate. SEM images confirm that the electrodes are fully coated with the activated $Cs_3Bi_2I_9$ layer (Figures 2a, 2b) , with crystalline $Cs_3Bi_2I_9$ both accumulating on the surface of the electrodes (Figure 2d) and directly coating individual carbon cloth fibres (Figure 2c). Despite their irregular orientation on the carbon cloth, the $Cs_3Bi_2I_9$ crystals roughly all adopt polygonal shapes, indicating that the simple fabrication process synthesized a $Cs_3Bi_2I_9$ coating with consistent crystal morphology. Although the SEM images indicate that the electrodes are predominantly coated with $Cs_3Bi_2I_9$ crystals, PTFE and charcoal are common additives used to strengthen the mechanical binding of the $Cs_3Bi_2I_9$ to the carbon cloth and to enhance the conductivity of the electrode surface, respectively.

To construct the supercapacitor device, a microporous polymer membrane (Celgard 3501) was first submerged in a saturated aqueous $NaClO_4$ electrolyte. The lightly soaked separator was then sandwiched between two of the coated electrodes (Figure 3a), and the entire assembly was packed and firmly compressed in a supercapacitor test cell without any further pretreatment for electrochemical analysis. The open circuit potential of the as-built supercapacitor was found to be 0.021 V, suggesting a high degree of symmetry in the constructed electrodes.

2.2 Evaluating charge storage mechanisms through cyclic voltammetry and galvanostatic charge-discharge cycles

We evaluated the electrochemical behavior and capacitive performance of the $Cs_3Bi_2I_9$-based supercapacitor in varying voltage and time regimes through cyclic voltammetry (CV) and galvanostatic charge-discharge measurements, aiming to identify its primary charge storage mechanisms. Figure 3b depicts the CV curves of the supercapacitor device in a voltage

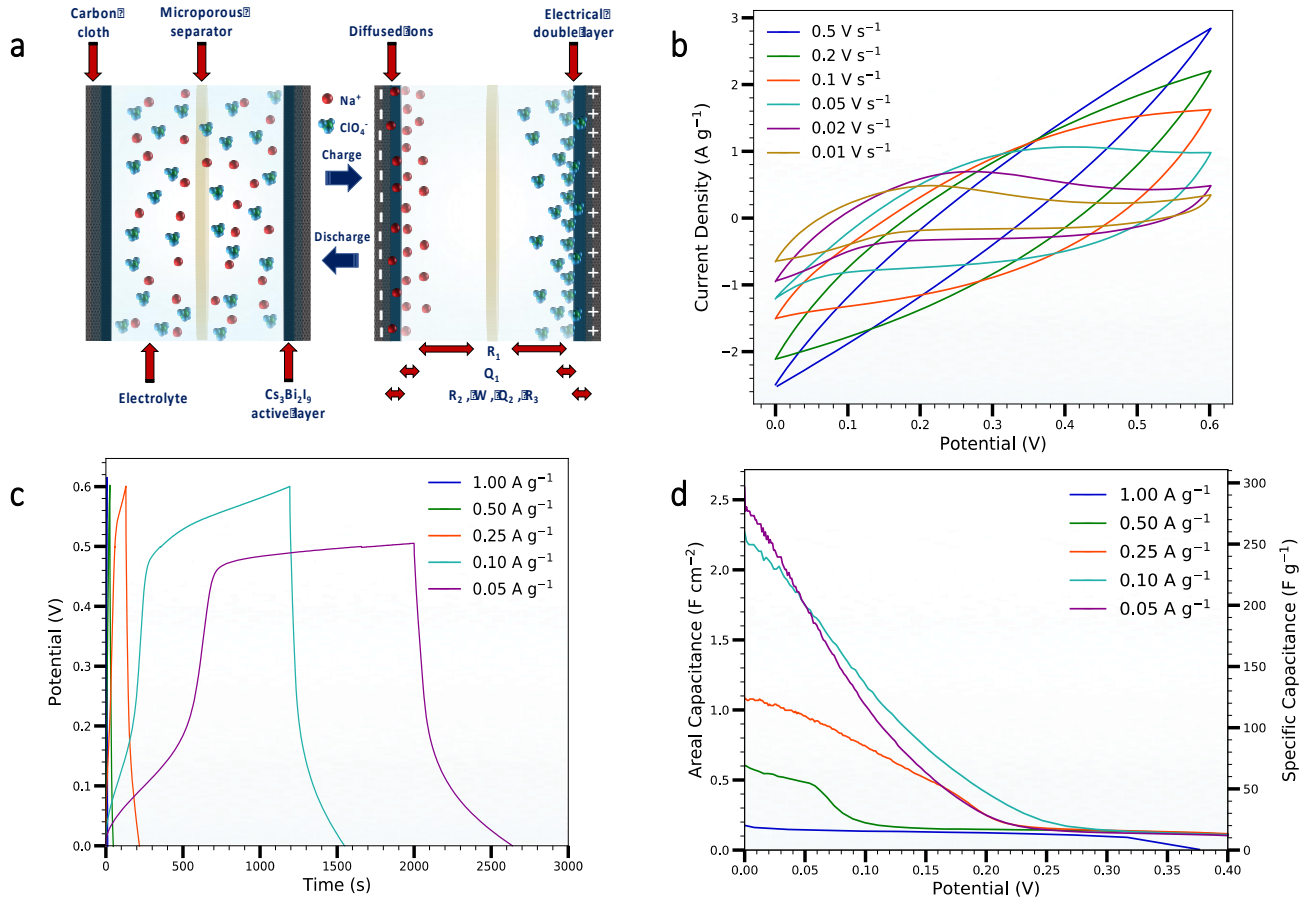

Figure 3. (a) Schematic of the assembled supercapacitor device. (b) Cyclic voltammograms of the supercapacitor at scanning rates of 500, 200, 100, 50, 20, and 10 mV s^{-1}. (c) Galvanostatic charge-discharge curves at selected current densities of 1.0, 0.5, 0.25, 0.1, and 0.05 A g^{-1}. (d) Instantaneous areal and specific capacitance of the supercapacitor versus the potential, calculated from the galvanostatic discharge curves according to Equations 2a and 2b.

window of 0.0 – 0.6 V at linear scan rates varying from 0.5 V s^{-1} to 0.01 V s^{-1}. For the fastest sweeps, the rapidly increasing potential produces sharp oval-shaped CV curves with steep slopes characteristic of resistive rather than capacitive responses.[33] Namely, during ultrafast scans, the electrolytic Na^+ and ClO_4^- ions have insufficient time to polarize, migrate, and form the electrostatic double layers at the surface of the $Cs_3Bi_2I_9$ electrodes, instead conducting current through resistive pathways. At intermediate scan rates, however, the CV curves plateau to develop rounded and peakless rectangular shapes characteristic of EDLC-type capacitors that store charge through electrostatic double layers between the coated electrodes and the polarized electrolyte (Figure 3a). Finally, at the lowest scan rates, the electrolytic ions have time to penetrate and diffuse into the surface pores of the activated $Cs_3Bi_2I_9$ layer and adsorb/desorb Faradaically to the surface and near-surface pockets of the electrodes, producing the broad and weak peaks extending from 0.0 to 0.2 V. The systemic areal (F cm^{-2}) and specific (F g^{-1}) capacitances for the $Cs_3Bi_2I_9$ supercapacitor were calaculated from the CV curves according to:

$$C_{areal} = \frac{\int_{\Delta V} i\,dV}{\Delta V \times s \times A} \qquad (1a)$$

$$C_{specific} = \frac{\int_{\Delta V} i\,dV}{\Delta V \times s \times m} \qquad (1b)$$

where i is current (A), ΔV is the voltage window of the cathodic (negative) current (V), s is the linear scan rate (V s^{-1}), A is the average geometric area of both electrodes (cm^2) of the two-electrode system, and m is the total mass (g) of the activated $Cs_3Bi_2I_9$ material coating both electrodes. We report both the areal and specific capacitances to more thoroughly evaluate the electrochemical charge storage capabilities of the $Cs_3Bi_2I_9$ supercapacitor. The device's systemic areal and specific capacitances were found to increase from 23 mF cm^{-2} to 200 mF cm^{-2} and from 2.6 F g^{-1} to 23 F g^{-1} for scan rates decreasing from 0.5 V s^{-1} to 0.01 V s^{-1}, confirming that the device displays enhanced capacitive behaviour for the slower charge-discharge sweeps (Figure S1, Supporting Information). When the voltage window for the CV scans was limited to 0.3 – 0.5 V (Figure S2a), the CV curves display ideal rounded rectangular shapes without any Faradaic peaks even at the lowest scan rate of 0.01 V s^{-1}. These limited CV

sweeps yield systemic areal and specific capacitances ranging from 8.3 mF cm^{-2} to 110 mF cm^{-2} and 0.95 F g^{-1} to 13 F g^{-1}, suggesting that the majority of the supercapacitor's capacity derives from its non-Faradaic, EDLC-type charge storage mechanism (Figure S2b).

In addition to cyclic voltammetry, galvanostatic charge-discharge measurements were conducted to evaluate the $Cs_3Bi_2I_9$ supercapacitor in a setting directly analogous to industrial applications of supercapacitors. Figure 3c depicts the galvanostatic charge-discharge measurements taken in a voltage window of 0.0 – 0.6 V with current densities ranging from 1 A g^{-1} to 0.05 A g^{-1}. Current densities are reported in amps per gram of total active material on both electrodes. Like the CV scans, the galvanostatic charge-discharge curves display both time and voltage dependent behaviour. At the highest current densities, the charge-discharge curves are largely symmetrical and triangular (Figure S3), characteristic of highly reversible and non-Faradaic charge adsorption/desorption at the electric double layer. At lower current densities, however, the charge-discharge curves exhibit markedly variable slopes dependent on the potential. During the initial charge cycle around 0.0-0.2 V, the galvanostatic curves adopt relatively low slopes corresponding to Faradaic electron transfer with ion adsorption/desorption in the surface and near-surface pores of the $Cs_3Bi_2I_9$-coated electrode. Whereas the initial slopes of EDLC galvanostatic charge-curves are typically steep and caused by the rapid formation of the electric double layer, the fact that our device's galvanostatic charge-discharge slopes are flattened during the initial charging suggests that Faradaic charge adsorption and pore-penetration is favoured at low potentials. From 0.2 V to 0.4 V, the slope steepens, attributed to non-Faradaic charge accumulation at the electrolyte/electrode interface. Finally, above 0.45 V the galvanostatic curve plateaus, showing again Faradaic behaviour at higher potentials. During discharge, the steep slope from 0.4 V to 0.2 V corresponds to the quick dissipation of the electric double layer as electrolytic ions shuttle away from the surface of the electrodes, whereas the flattened slope from 0.2 V to 0.0 V corresponds to kinetically-limited Faradaic desorption as well as slow ion diffusion out of the electrodes' pores. The systemic areal and specific capacitances were calculated from the slope of the discharge curves according to:

$$C_{areal} = \frac{i}{\frac{dV}{dt} \times A} \qquad (2a)$$

$$C_{specific} = \frac{i}{\frac{dV}{dt} \times m} \qquad (2b)$$

where i is the constant applied current, $\frac{dV}{dt}$ is the slope of the discharge curve, and A and m retain their definitions from Equation 1. Given the variability of the slopes of the discharge curves, rather than report a single value of the capacitance derived from the galvanostatic curves, Figure 3d presents the instantaneous areal and specific capacitances versus the potential, calculated using Equations 2a and 2b. We simply note that the $Cs_3Bi_2I_9$ supercapacitor attained maximum systemic areal and specific capacitances of 2.4 F cm^{-2} and 280 F g^{-1} at the lowest tested current density of 0.05 A g^{-1}. Although the true device areal capacitance likely sits intermediate between the CV-derived capacitance of 200 mF cm^{-2} and the galvanostatic-derived capacitance of 2.4 F cm^{-2}, our $Cs_3Bi_2I_9$ supercapacitor undoubtedly attains an areal capacitance approximately 100 to 1000 times greater than the already high single-electrode areal capacitance of 5.5 mF cm^{-2} (equivalent to a systemic areal capacitance of 2.25 mF cm^{-2}, since the electrodes are symmetric and connected in series) achieved by the $(CH_3NH_3)Bi_2I_9$-based EDLC reported by Pious and colleagues. Their $(CH_3NH_3)Bi_2I_9$-based EDLC was also prepared through a solution-deposition procedure (using ethanol rather than DMF) and featured a similar device architecture, albeit with a different electrolyte (methylammonium iodide/butanol rather than aqueous $NaClO_4$).[30] The superior energy storage capabilities of our $Cs_3Bi_2I_9$—based supercapacitor are possibly due to higher surface coverage of the electrodes and the Faradaic charge adsorption/desorption processes potentially promoted by the $NaClO_4$ electrolyte (see Figure S4 for Ragone Plot). We note also the non-flammability of the electrolyte used in our case. Regardless, the remarkable electrochemical performance of $Cs_3Bi_2I_9$ warrants further optimization and implementation in commercial applications.

2.3 Long-term cycle stability of the $Cs_3Bi_2I_9$ electrodes

The long-term cycle stability and capacitance retention of the $Cs_3Bi_2I_9$-based supercapacitor were evaluated by measuring the fluctuation in capacitance over 5000 galvanostatic charge-discharge cycles at a high current density of 1.0 A g^{-1}. Figure 4a displays the remarkable overall capacitive stability of the $Cs_3Bi_2I_9$ electrodes, normalized with respect to the initial capacitance of the first charge-discharge cycle. After an initial increase in capacitance likely caused by electrical conditioning of the electrodes' surface to be more receptive to ion adsorption/desorption, the capacitance retention gradually decreases to 88% of the original value after the full 5000 cycles, only dropping below 100% after 1800 cycles. Moreover, the open circuit potential of the $Cs_3Bi_2I_9$-based supercapacitor increased only slightly from 0.047 V to 0.090 V, suggesting that the electrodes underwent minimal surface re-organisation over the cycling period. This excellent capacitive stability is confirmed by the XRD pattern of the post-cycled electrodes, which is compared against the untested electrodes in Figure 4b. Despite the intense electrical conditions, the persistent and strong peaks near $2\theta = 25^o, 26^o$, 27^o and 30^o prove that the $Cs_3Bi_2I_9$ active layer retains its crystal morphology with little chemical degradation over the

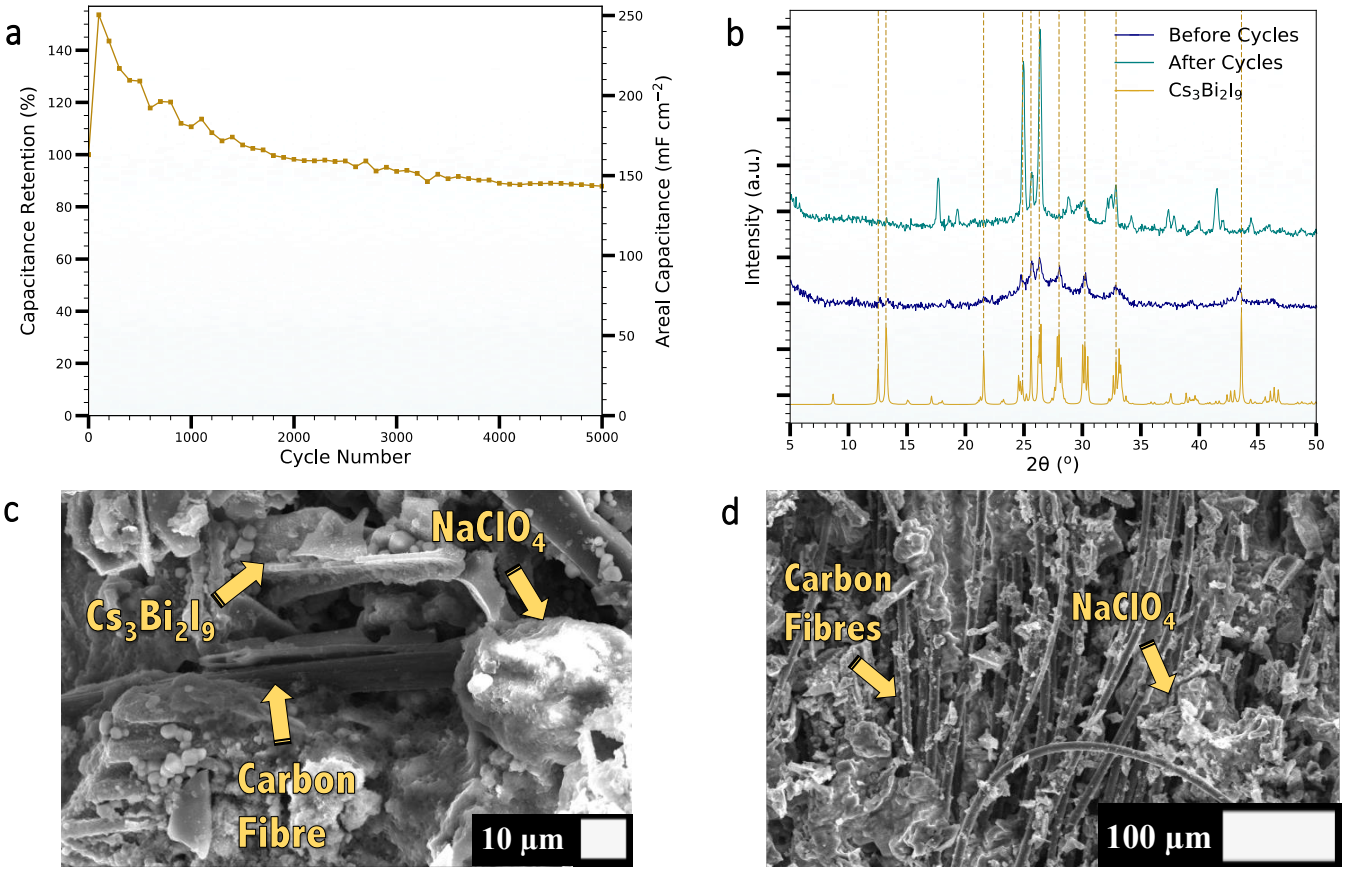

Figure 4. (a) Capacitance retention of the $Cs_3Bi_2I_9$ – based supercapacitor over 5000 galvanostatic charge-discharge cycles at a current density of 1.0 A g^{-1}. (b) XRD pattern of the electrode surface before (blue) and after (green) the 5000 cycles, compared with the powder $Cs_3Bi_2I_9$ pattern (gold) calculated from CCDC Mercury software (ICSD data base for coll. code 1448)[32]. (c) and (d) SEM images of the electrodes after undergoing 5000 charge-discharge cycles.

5000 cycles. The additional peaks at 17.5° and 42° are caused by crystallized $NaClO_4$ electrolyte heavily coating the post-cycled electrodes (Figure 4c, 4d). Moreover, SEM images of the post-cycled electrodes verify that the $Cs_3Bi_2I_9$ crystals, although obscured by the crystalized $NaClO_4$, largely retain their polygonal plate-like morphology (Figure 4c), suggesting high integrity of the $Cs_3Bi_2I_9$ crystal structure. In addition to XRD, Raman spectra taken of the $Cs_3Bi_2I_9$ electrodes pre- and post-cycles testing show essentially identical chemical bond vibrational Raman shifts despite the 5000 cycles (Figure S5). We note that little information can be obtained from the Raman spectra apart from the qualitative agreement between the pre- and post-cycled spectra, as surface irregularity and unevenness of the electrodes impedes ideal scattering of the Raman laser light, decreasing the signal to noise ratio. Overall, the stable crystal morphology and excellent 88% capacitance retention of the $Cs_3Bi_2I_9$ prove its potential as a stable, high-achieving supercapacitor electrode material.

2.4 Electrochemical impedance spectroscopy

Electrochemical impedance spectroscopy (EIS) is a powerful analytical tool used to investigate the resistive and capacitive behaviours of electrochemical systems in response to AC current oscillating about a given potential at variable frequencies. Typically, the EIS data are fitted to an equivalent circuit model wherein each circuit element corresponds to a physical process in the electrochemical device. Analysing both the circuit itself and the individual circuit elements can provide detailed information on the ohmic loss, charge transfer, and mass transport in the supercapacitor.[34,35] In this study, we performed EIS at an AC amplitude of ± 10 mV at both open circuit potential (OCP) and 0.4 V to more thoroughly understand the physical origin of the time-dependent shapes of the CV and galvanostatic charge-discharge curves. All EIS measurements were taken at frequencies ranging from 150 kHz to 0.01 Hz.

Figure 5a shows the real/in-phase impedance versus the imaginary/out-of-phase impedance in a so-called Nyquist plot of the $Cs_3Bi_2I_9$ supercapacitor at an OCP of 0.083 V. This OCP is within the 0.0-0.2 V range displaying Faradaic behaviour in the CV and galvanostatic charge-discharge cycles, and thus

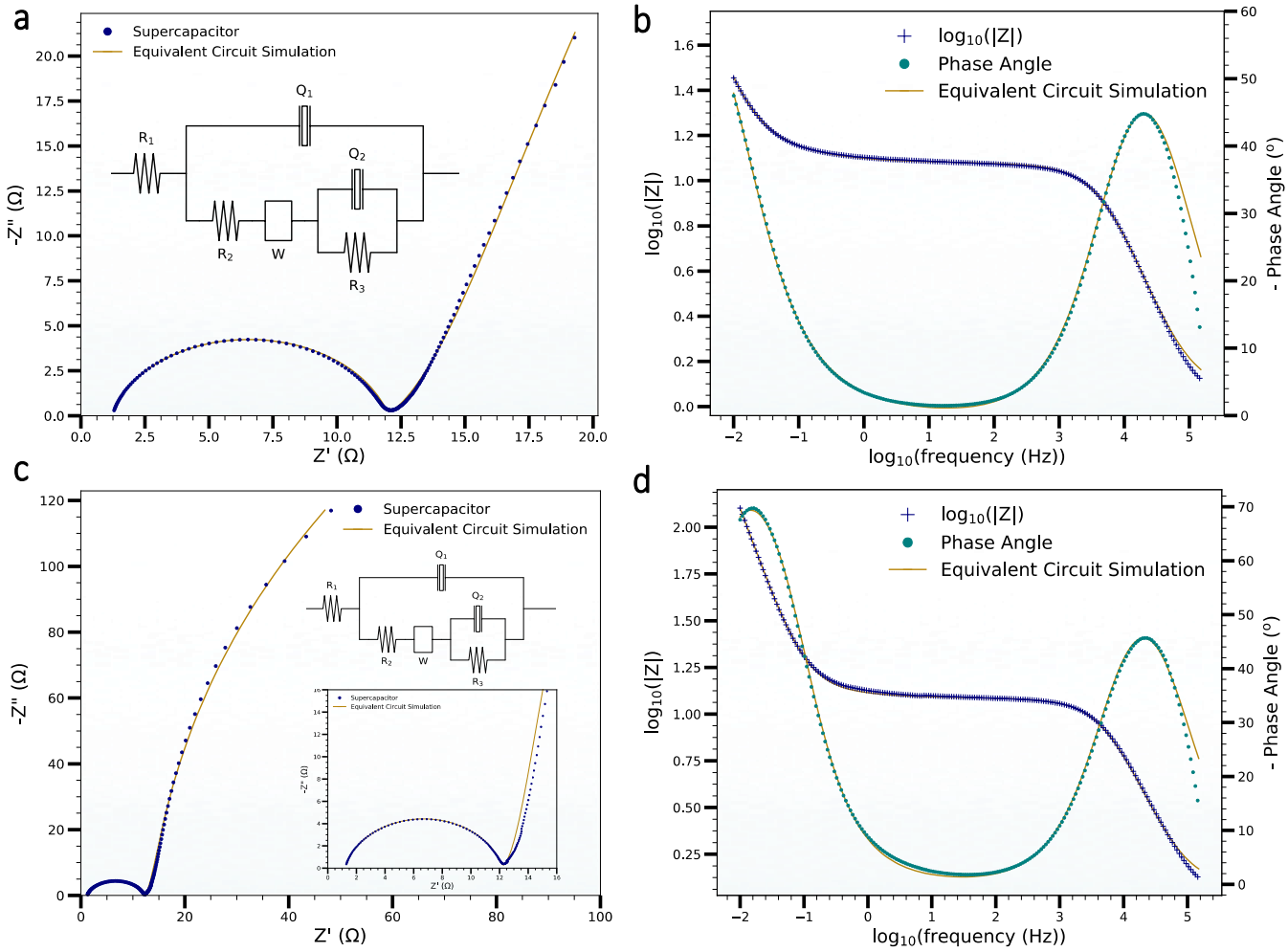

Figure 5. (a) Nyquist plot for the supercapacitor taken at the open circuit potential of 0.083 V (blue) with the fitted spectrum (gold) simulated from the inserted equivalent circuit. (b) Bode plot of the supercapacitor taken at OCP (blue, green) with the simulated Bode plot (gold). (c) Nyquist plot for the supercapacitor taken at a potential of 0.4 V (blue) with the fitted spectrum (gold) simulated from the inserted equivalent circuit. (d) Bode plot of the supercapacitor taken at 0.4 V (blue, green) with the simulated Bode plot (gold).

we interpret the EIS results as arising from the supercapacitor's pseudocapacitive behaviour. While the Nyquist plot itself does not indicate the frequency at which the impedance values were measured, the Bode plot for the same EIS data plots both the absolute value of the complex impedance and the phase angle of the impedance versus the log frequency (Figure 5b) . Both the Nyquist and Bode plots were used to simulate the accompanying equivalent circuit, shown as an inset in Figure 5a with circuit element values and fitting errors reported in Table 1. The Nyquist plot at OCP displays standard supercapacitor behaviour with a depressed semi-circle in the high-frequency regime and linear behaviour in the low-frequency regime. At the highest frequencies, the electrolytic Na^+ and ClO_4^- ions have insufficient time to polarize and form the electrical double layer at the surface of the electrodes, and the resulting semi-circle begins to form with an intercept on the Z' axis corresponding to the combined resistance of the electrolyte and the current collectors of the supercapacitor assembly. Because all charge-transfer in the electrochemical cell occurs through the electrolyte, this resistance is simulated in series as R_1 with a value of 1.159 Ω (Table 1). At high to mid frequencies, the electrolyte fully polarizes to form the electrostatic double layers, and the resulting Nyquist semi-circle emerges to account for two possible charge pathways in the supercapacitor: the ions either accumulate at the surface of the electrodes, forming an EDLC capacitor, or diffuse into the surface pores. The curvature of the high-frequency depressed semi-circle represents the EDLC formation at the easily-accessible surface of the electrodes and is modelled by Q_1, a constant phase element (CPE) with both an ideality factor n, indicating an imperfect capacitor, and an admittance parameter Y_0. Q—Y_0 is related to capacitance and is given by:

$$Z = \frac{1}{(Y_0 j\omega)^n} \quad (3)$$

where Z is the impedance of the CPE, ω is the radial frequency (rad s^{-1}), $j = \sqrt{-1}$, and n is the ideality factor. Although Y_0 has precise units of $(F\, s^{n-1})^{1/n}$, Y_0 is often erroneously reported in Farads, which is only true in the case of a perfect capacitor (n = 1).[36] For accuracy, we will report Q—Y_0 with its proper units of $(F\, s^{n-1})^{1/n}$, except in the limiting case n = 1. At OCP = 0.083 V, the $Cs_3Bi_2I_9$ supercapacitor was found to have a ideality factor n = 0.847 and a Q_1—Y_0 of 14.05 $\mu(F\, s^{-0.153})^{1.18}$. The non-ideality of the capacitor is likely due to a non-uniform, porous electrode surface,[37] which is evident from the SEM images of the electrode surface (Figure 2), while Q_1's relatively low Y_0 is standard of purely electrostatic capacitors. Q_1 is fitted in parallel with R_2 = 10.80 Ω, which corresponds to the diameter of the semi-circle and models both the charge-transfer resistance and adsorption resistance of the electrode/electrolyte interface during the diffusion of the ions into the electrodes' pores. Because the $Cs_3Bi_2I_9$-based supercapacitor adopts pseudocapacitive as well as EDLC behaviour at 0.083 V and because of Q_1's limited Y_0, $R_1 + R_2$ = 11.96 Ω represents the equivalent series resistance (ESR) of the device. Such a small ESR suggests a high degree of surface conductivity and limited ohmic loss through the $Cs_3Bi_2I_9$ electrodes and electrolyte, which is preferable for excellent overall performance of the supercapacitor. To model the diffusion-controlled mass transport of the Na^+ and ClO_4^- through the electrodes' pores at mid to low frequencies (1-100 Hz), the Warburg impedance element W is fitted in series with R_2 with a Y_0 parameter of 0.472 $\Omega^{-1}\, s^{1/2}$, equal to the admittance at a radial frequency of 1 rad s^{-1}. W—Y_0 can then be used to calculate the Warburg diffusion coefficient σ according to:

$$\sigma = {}^{1}/_{\sqrt{2}\,Y_0} \quad (4)$$

Typically, a Warburg element will produce linear behaviour in the Nyquist plot at mid to low frequencies with a slope of 45°. The experimental data, on the other hand, shows a line with a slope of approximately 73° below 1 Hz. This steeper slope suggests that the Warburg diffusion is in series with a second capacitor, modelled as the constant phase element Q_2 with a high ideality factor n = 0.994 and an ultrahigh Y_0 of 1.012 $(F\, s^{-0.0064})^{1.006}$. This high Y_0 is in close agreement with the areal capacitances calculated from the CV and galvanostatic curves and corresponds to Faradaic ion adsorption/desorption at the electrode surface and in the inner pores of the electrodes. Q_2 is in parallel with a third resistor R_3 to account for resistive losses during Faradaic electron transfer as well as for trapped ions during discharge. R_3 is fitted with much higher resistance of 195.5 Ω, suggesting that the majority of charge is stored in Q_2 rather than lost through resistive channels. We note that R_3 would produce a second, much larger semi-circle at ultralow frequencies. Because the frequency range is limited to 0.01 Hz, this semi-circle does not form, which in turn leads to the large error (10.3%) in the fit for R_3.

Table 1. Circuit element values and non-linear least squares fitting errors for the simulated equivalent circuit shown in Figure 5. Values and errors are given for the EIS data taken before the 5000 charge-discharge cycles at both OCP = 0.083 V (Figures 5a, 5b) and 0.4 V (Figures 5c, 5d).

Circuit Element	Value (OCP)	% Error	Value (0.4 V)	% Error
R_1	1.159 Ω	1.514	1.202 Ω	3.672
$Q_1 - n$	0.847	0.253	0.865	0.617
$Q_1 - Y_0$	14.05 $\mu(F\, s^{-0.153})^{1.18}$	2.046	11.00 $\mu(F\, s^{-0.135})^{1.16}$	5.126
R_2	10.80 Ω	0.199	10.95 Ω	0.491
W – Y_0	0.4722 $\Omega^{-1}\, s^{1/2}$	1.640	0.388 $\Omega^{-1}\, s^{1/2}$	3.265
$Q_2 - n$	0.9936	0.712	1.00	0.219
$Q_2 - Y_0$	1.012 $(F\, s^{-0.0064})^{1.006}$	2.488	0.1363 F	0.820
R_3	195.5 Ω	10.337	465 Ω	1.264

In addition to conducting EIS at open circuit potential, EIS was also performed at a potential of 0.4 V, where the CV curves display purely non-Faradaic behaviour (Figure S2a). Figures 5c and 5d display the Nyquist and Bode plots for the EIS spectrum of the $Cs_3Bi_2I_9$ supercapacitor at 0.4 V. Whereas the scheme of the simulated equivalent circuit is identical to that for the open circuit potential EIS spectrum, the individual circuit elements' values have changed to reflect the different electrical conditions (Table 1). Changing the potential from 0.083 V to 0.4 V had little effect on the supercapacitor's behaviour at high-frequencies, with R_1 increasing slightly to 1.202 Ω, Q_1 decreasing in both ideality (n = 0.865) and Y_0 (11.00 $\mu(F\, s^{-0.135})^{1.16}$) and R_2 marginally increasing to 10.95 Ω. The supercapacitor's response to the mid to low frequency AC current, however, did change dramatically with the new potential. W—Y_0 decreased to 0.388 $\Omega^{-1}\, s^{1/2}$, Q_2's ideality increased to n = 1.00 (a perfect capacitor) while its capacitance Y_0 dropped dramatically to 0.136 F, and R_3 increased to 465 Ω. Because the Warburg impedance is inversely proportional to W—Y_0, a decrease in W—Y_0 corresponds to increasingly impeded diffusion of the electrolyte into the electrodes' surface. This hindered diffusion, probably caused by the applied potential disfavouring pseudocapacitive adsoprtion/desportion, likely impedes ion adsorption/desorption and prevents electron transfer, decreasing the Y_0 of Q_2. We note that Q_2's capacitance Y_0 = 0.136 F matches the areal capacitance derived from the CV curves measured in a limited voltage window of 0.3 – 0.5 V, corroborating our interpretation that the $Cs_3Bi_2I_9$'s primary charge storage mechanism switches from pseudocapacitive to non-Faradaic and electrostatic when the potential increases from 0.0 – 0.2 V to 0.3 – 0.5 V. Finally, we attribute the increased R_3, which is in parallel with Q_2, to

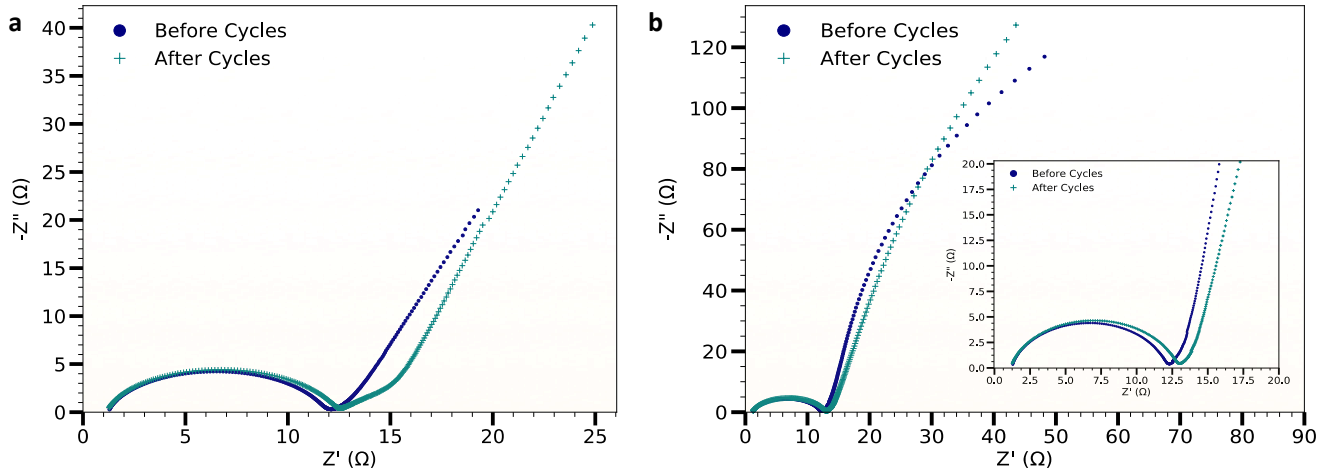

Figure 6. Nyquist plots for the supercapacitor taken both before (blue) and after (green) the 5000 charge-discharge cycles, taken at (a) the open circuit potentials of 0.083 V and 0.090 V, respectively, and (b) 0.4 V each.

fewer resistive losses during the non-Faradaic ion adsorption/desorption processes within the electrode pores.

2.5 EIS characterization of long-term electrode durability

Electrochemical impedance spectroscopy was also used to re-characterize the resistive and capacitive channels in the $Cs_3Bi_2I_9$ supercapacitor after the 5000 galvanostatic charge-discharge cycles were performed in order to evaluate the electrodes' long-term durability. Figures 6a and 6b compare the EIS Nyquist spectra both at open circuit potential (6a) and 0.4 V (6b) before and after the 5000 cycles. The pre-cycles spectra are the same as those in Figure 5. The same equivalent circuit as simulated in Figure 5 was fitted to the post-cycles spectra at OCP = 0.090 and 0.4 V (Figure S6) with circuit element values and errors tabulated in Table S1, while Table 2 reports the difference between the post- and pre- cycles circuit element values for easy comparison. For the Nyquist before/after plots both at OCP = 0.090 V and 0.4 V, the circuit elements responded in qualitatively identical ways to the 5000 charge-discharge cycles. R_1 decreased by slightly over 0.1 **Ω** in both cases, while Q_1 increased slightly in Y_0 but dropped marginally in ideality. Both responses are likely due to the same surface re-organisation of the porous electrodes' surfaces as was deduced from the increased capacitance in the first 1800 galvanostatic charge-discharge cycles (Figure 3a). R_2 also increased by about 0.8 – 0.9 **Ω** for both potentials, which may correspond to minor weathering of the electrodes' active material and greater surface roughness and irregularity that increased the charge transfer resistance within the electrode/electrolyte interface. A marked decrease in the W—Y_0 parameter by approximately 0.1 – 0.2 Ω^{-1} $s^{1/2}$ indicates slower diffusion of the electrolyte in and out of the electrodes' pores, possibly due to increased surface roughness, reduced pore size, or trapped ions. While the ideality factor of Q_2 did not change significantly after the 5000 cycles in both cases, the Q_2 — Y_0 dropped by nearly 50% for the OCP trial but remained largely constant for the 0.4 V trial. Because the OCP trial was taken in the pseudocapacitive voltage regime of the $Cs_3Bi_2I_9$ supercapacitor, we attribute this one-sided decrease in Q_2 — Y_0 to both inhibited ion diffusion and minor irreversible Faradaic reactions occurring at the electrodes' surfaces. Finally, R_3 increased by a drastic 200-500 **Ω** for both EIS spectra, which we again attribute to film conditioning that reduced ohmic loss across the electrodes after numerous charge-discharge cycles. Overall, the resistive elements of the supercapacitor's electrodes and electrolyte either improved or remained relatively unchanged across the 5000 cycles, while only the pseudo-capacitance dropped meaningfully. We thus reemphasize the long-term cycle stability of $Cs_3Bi_2I_9$ as the active electrode material in supercapacitor devices.

3. Conclusions

We have fabricated a supercapacitor utilizing $Cs_3Bi_2I_9$ as the active electrode material and aqueous $NaClO_4$ as the electrolyte from an economical and solution-processable route. XRD and SEM characterization of the coated electrodes indicate excellent surface coverage of the carbon cloth substrate with highly crystalline and pure $Cs_3Bi_2I_9$. We have evaluated the energy storage capabilities of the $Cs_3Bi_2I_9$-based supercapacitor through cyclic voltammetry and galvanostatic charge-discharge curves, and we have thoroughly characterized the time and voltage-dependent charge storage mechanisms of the device with cyclic voltammetry and electrochemical impedance spectroscopy. The supercapacitor was found to have maximum areal and specific capacitances of 2.4 F cm^{-2} and 280 F g^{-1}, representing an outstanding 1000-

fold improvement upon a previously reported $(CH_3NH_3)_3Bi_2I_9$-based device. The long-term cycle stability and electrode durability of the supercapacitor was evaluated by performing 5000 galvanostatic charge-discharge cycles at a current density of 2 A g^{-1} and by assessing the electrodes' structural and electrochemical integrity with XRD and EIS. The $Cs_3Bi_2I_9$ device was found to retain a commendable 88% of its original capacitance across the 5000 cycles. Given that this is the first report of a completely new active material, such outstanding capacitive performance and long-term stability prove $Cs_3Bi_2I_9$ to be an excellent material for supercapacitor applications, which can still undergo much further optimisation of the morphology, electrolyte, current collector and overall device geometry towards potential commercialization.

4. Experimental Methods

4.1 Materials

N, N-Dimethylformamide (anhydrous, 99.8%), bismuth(III) iodide (99%), poly(tetrafluoroethylene) powder (1 μm particle size), and activated charcoal (CAS: 7440-44-0) were purchased from Sigma-Aldrich, and caesium iodide was obtained from BDH Chemicals Ltd Poole England. All reagents were used as received unless otherwise stated.

4.2 Preparation of $Cs_3Bi_2I_9$ electrodes

A 3:1 molar mixture of CsI:BiI_3 was mixed with activated charcoal and PTFE powder in an 85:10:5 weight ratio (76.1 mg CsI, 115.1 mg BiI3, 22.5 mg charcoal, 11.25 mg PTFE), and the entire mixture was dissolved and dispersed in DMF (1.0 mL) to form a suspended solution. After sonicating, approximately 200 μL of the as-prepared solution was drop-cast onto 1 cm^2 sections of carbon cloth (NuVant Systems Inc., ELAT Hydrophilic) laying on top of tissue paper, which served to absorb excess solution. The soaked carbon cloth squares were then transferred to a Pyrex petri dish and annealed at 150 °C on a hot plate for 1 hour. The dried electrodes were then trimmed, weighed, and measured under an optical microscope. The electrodes used in this study had dimensions of 9.0 mm x 9.7 mm and 9.5 mm x 9.6 mm, and an average mass loading of activated $Cs_3Bi_2I_9$ material of 3.9 mg cm^{-2} per electrode (a total of 7.8 mg of $Cs_3Bi_2I_9$ on both electrodes). The mass of the active layer was calculated by subtracting the mass of the underlying carbon cloth (areal density = 13 mg cm^{-2}) from the measured mass of the electrodes. To circumvent inaccuracies in measuring the low mass of active material deposited on the carbon cloth electrodes, we report both areal and gravimetric specific capacitances, and we report all specific capacitances with only two significant figures. For comparison, control experiments were performed using the same cell, electrolyte and current collector, but without the active material (Table S2) and these typically showed values around two orders of magnitude lower.

4.3 Assembly of supercapacitor

To assemble the $Cs_3Bi_2I_9$-based supercapacitor, a circular section (>1 cm^2) of a thin microporous polymer membrane (Celgard 3501, 25 μm) was briefly soaked in a saturated aqueous $NaClO_4$ solution and sandwiched between two as-prepared electrodes. The electrode/separator/electrode stack was then packed into a standard electrochemical cell (ECC-std, EL-CELL GmbH) and tightly compressed to minimize separation between the electrodes and electrolyte-soaked membrane.

Table 2. Change (Δ) in the value of each simulated circuit element after 5000 charge-discharge cycles for the EIS data taken at both OCP and 0.4 V (Figure 6). Note that the Δ (Q—Y_0) values are more qualitative than strictly quantitative and are presented without units, as the units of Q—Y_0, $(F\ s^{n-1})^{1/n}$, vary with Q—n.

Circuit Element	Δ (OCP)	Δ (0.4 V)
R_1	-0.146 Ω	-0.114 Ω
$Q_1 - n$	-0.0239	-0.0211
$Q_1 - Y_0$	+2.25 x 10^{-6}	+3.23 x 10^{-6}
R_2	+0.79 Ω	+0.88 Ω
$W - Y_0$	-0.213 Ω^{-1} $s^{1/2}$	-0.1329 Ω^{-1} $s^{1/2}$
$Q_2 - n$	+0.0064	+0.00
$Q_2 - Y_0$	-0.4717	-0.0013 F
R_3	+521.5 Ω	+193 Ω

4.4 Electrochemical testing

Electrochemical analysis was performed by connecting the as-assembled supercapacitor test cell in a two-electrode configuration to an Autolab potentiostat with the FRA2 module. Cyclic voltammetry and galvanostatic charge-discharge measurements were conducted using the General Purpose Electrochemical System software (GPES, version 4.9.007), and electrochemical impedance spectroscopy was carried out using Frequency Response Analyser (FRA, version 4.9.007) software. Equivalent circuit fitting was conducted using FRA's Fit and Simulation software (version 1.7).

4.5 Electrode characterization

X-Ray diffraction (XRD) was conducted on a Bruker (D2 Advance) diffractometer utilizing monochromatic Cu-Kα radiation (wavelength 1.5406 Å) at room temperature. XRD scans were performed at scattering angles ranging from 5° to 60° with 0.05° increments on a 2-theta scale. Raman spectroscopy was performed on a Renishaw InVia Raman Microscope (wavelength 785 nm, spectral resolution 1 cm^{-1}).

SEM images were acquired from JEOL JSM-6010PLUS/LV scanning electron microscope, with an electron beam accelerating voltage of 10 kV using secondary electron imaging. $Cs_3Bi_2I_9$ – coated carbon cloth was placed directly onto sticky carbon pad, which was subsequently positioned on a sample holder.

Acknowledgements

We thank the EPSRC Multiscale Tuning of Interfaces and Surfaces for Energy Applications consortium for a flexible-funding project (Open data at: doi.org/10.7488/ds/2542), and the University of Edinburgh, School of Chemistry for financial support. We thank Dr. Andrey Gromov for performing the Raman spectroscopy measurements. We thank the EPSRC SOFI CDT and Dr. Andrew Schofield for assistance with the SEM imaging. We thank Prof. Andrew Mount for the invaluable discussion concerning supercapacitors. KA thanks the University of Edinburgh – University of Chicago Chemistry Exchange Program and the University of Chicago SITG grant for administrative and financial support.

References

[1] M. C. Argyrou, P. Christodoulides, S. A. Kalogirou, *Renewable and Sustainable Energy Reviews*, 2017, **94,** 804-821
[2] M. Hannan, M. Hoque, A. Mohamed, A. Ayob, *Renewable and Sustainable Energy Reviews*, 2016, **69**, 771-789
[3] N. Sulaiman, M. Hannan, A. Mohamed, E. H. Majlan, W. R. Wan Daud, *Renewable and Sustainable Energy Reviews*, 2015, **52,** 802-814
[4] J. Miller, P. Simon, *Science Magazine*, 2008, **321**, 651-652
[5] G. Z. Chen, *International Materials Reviews*, 2017, **62**, 173-202
[6] M. Bakker, R. Frazier, S. Burkett, J. E. Bara, N. Chopra, S. Spear, S. Pan, C. Xu, *Nanomaterials and Energy*, 2012, **1,** 136-158
[7] M. Winter, R. Brodd, *Chemical Reviews*, 2004, **104**, 4245-4269
[8] W. Zuo, R. Li, C. Zhou, Y. Li, J. Xia, J. Liu, *Advanced Science*, 2017, **4**, 1-21
[9] Y. Wang, Y. Song, Y. Xia, *Chemical Society Reviews*, 2016, **45**, 5925-5950
[10] Z. Yu, L. Tetard, L. Zhai, J. Thomas, *Energy and Environmental Science*, 2015, **8**, 702-730
[11] M. Yassine, D. Fabris, *Energies*, 2017, **10**, 1340
[12] P. Simon, Y. Gogotsi, *Nature Materials*, 2008, **7**, 845-854
[13] C. Cyrille, T. R. Porter, J. Savéant, *ACS Applied Materials & Interfaces*, 2017, **9**, 8649-8658
[14] B. E. Conway, V. Birss, J. Wojtowicz, *Journal of Power Sources*, 1997, **66**, 1-14
[15] Z. Han, S. Pineda, A. T. Murdock, D. H. Seo, K. K. Ostrikov, A. Bendavid, *Journal of Materials Chemistry A*, 2017, **5**, 17293-17301
[16] G. Ali, M. Yusoff, E. Shaaban, K. F. Chong, *Ceramics International*, 2017, **43**, 8440-8448
[17] J. Qin, Z. S. Wu, F. Zhou, Y. Dong, H. Xiao, S. Zheng, S. Wang, X. Shi, H. Huang, C. Sun, X. Bao, *Chinese Chemical Letters*, 2018, **29**, 582-586
[18] L. Liu, L. Su, J. Lang, B. Hu, S. Xu, X. Yan, *Journal of Materials Chemistry A*, 2017, **5**, 5523-5531
[19] J. H. Kim, C. Choi, J. M. Lee, M. J. de Andrade, R. H. Baughman, S. J. Kim, *Scientific Reports*, 2018, **8**, 13309
[20] Y. W. Lee, B. S. Kim, J. Hong, J. Lee, S. Pak, H. S. Jang, D. Whang, S. Whang, S. Cha, J. I. Sohn, J. M. Kim, *Journal of Materials Chemistry A*, 2016, **4**, 10084-10090
[21] X. Song, C. Huang, Y. Qin, H. Li, H. C. Chen, *Journal of Materials Chemistry A*, 2018, **6**, 16205-16212
[22] J. Hao, S. Peng, H. Li, S. Dang, T. Qin, Y. Wen, J. Huang, F. Ma, D. Gao, F. Li, G. Cao, *Journal of Materials Chemistry A*, 2018, **6**, 16094
[23] J. Wang, S. Dong, B. Ding, Y. Wang, X. Hao, H. Dou, Y. Xia, X. Zhang, *National Science Review*, 2017, **4**, 71-90
[24] R. Chen, I. Puri, I. Zhitomirsky, *Ceramics International*, 2018, **44**, 18007-18015
[25] Y. Gogotsi, P. Simon, *Science*, 2012, **334**, 917-918
[26] T. Li, Q. Wang, G. S. Nichol, C. A. Morrison, H. Han, Y. Hu, N. Robertson, *Dalton Transactions*, 2018, **47**, 7050-7058
[27] Z. Ma, S. Peng, Y. Wu, X. Fang, X. Chen, X. Jia, K. Zhang, N. Yuan, J. Ding, N. Dai, *Physica B: Condensed Matter*, 2017, **526**, 136-142
[28] M. Lyu, J. J. Yun, P. Chen, M. Hao, L. Wang, *Advanced Energy Materials*, 2017, **7**, 1602512
[29] S. Zhou, L. Li, H. Yu, J. Chen, C. P. Wong, N. Zhao, *Advanced Electronic Materials*, 2016, **2**, 1-8
[30] J. K. Pious, M. L. Lekshmi, C. Muthu, R. B. Rakhi, V. C. Nair, *ACS Omega*, 2017, **2**, 5798-5802
[31] K. Adams, A. F. González, J. Mallows, T. Li, J. H. J. Thijssen, N. Robertson, *Journal of Materials Chemistry A*, 2019, Advance Article
[32] C. F. Macrae, P. R. Edgington, P. McCabe, E. Pidcock, G. P. Shields, R. Taylor, M. Towler and J. van de Streek, *J. Appl. Cryst.*, 2006, **39**, 453-457
[33] A. Allagui, T. J. Freeborn, A. S. Elwakil, B. J. Maundy, *Scientific Reports*, 2016, **6**, 38568
[34] B. Mei, O. Munteshari, J. Lau, B. Dunn, L. Pilon, *The Journal of Physical Chemsitry C*, 2018, **122**, 194-206
[35] J. Kang, J. Wen, S. H. Jayaram, A. Yu, X. Wang, *Electrochimica Acta*, 2014, **115**, 587-598
[36] P. Żółtowski, *Journal of Electroanalytical Chemistry*, 1998, **443**, 149-154
[37] J. Jorcin, M. E. Orazem, N. Pébère, B. Tribollet, *Electrochimica Acta*, 2006, **51**, 1473-1479